Minerals Engineering 174 (2021) 107238

Contents lists available at ScienceDirect

Minerals Engineering

journal homepage: www.elsevier.com/locate/mineng

In situ high temperature spectroscopic study of liquid inclusions and hydroxyl groups in high purity natural quartz

Bartłomiej A. Gaweł [a,b], Anna Ulvensøen [a], Katarzyna Łukaszuk [b], Astrid Marie F. Muggerud [b], Andreas Erbe [a,*]

[a] Department of Materials Science and Engineering, NTNU, Norwegian University of Science and Technology, 7491 Trondheim, Norway
[b] The Quartz Corp, Strandveien 50, 1366 Lysaker, Norway

ARTICLE INFO

Keywords:
Quartz
Infrared (IR) spectroscopy
Raman spectroscopy
In situ thermal treatment
Multivariant curve resolution
Water
OH stretching modes
Hydroxyl groups
Silica

ABSTRACT

High purity natural based quartz is used as raw material for production of crucibles for solar-grade silicon production. The crucible properties are strongly related to presence of water and hydroxyl groups in the raw material. In this work, in situ temperature-dependent diffuse reflectance infrared (DRIFT) and Raman spectroscopy in the spectral range of the OH stretching modes, 3000–4000 cm^{-1}, were used to investigate water inclusions and hydroxyl groups at temperatures up to 800 °C. DRIFT shows that a substantial amount of liquid water was removed at 700 °C whereas new silanol groups characterised by stretching modes at about 3650 cm^{-1} were formed above 200 °C. A surface OH mode was also identified by multivariante curve resolution (MCR) of Raman maps. These surface OH groups were interpreted as the sign of formation of a hydrated layer at the surface of inclusions. It was not possible to detect water signals in other types of structural defect like cracks. Images were acquired in an in situ cell showing different stages of the rupture of an inclusion with a diameter of ≈8 μm between 400 and 500 °C. The in situ Raman spectrum of the inclusion water showed the typical liquid water bands at room temperature with a maximum moving to higher wavenumbers with increasing temperature. At 400 °C, the single peak at 3645 cm^{-1} indicated a situation close to the critical point, triggering rupture. The rupture of such large inclusions was thus identified as the dominating channel for the removal of liquid water inclusions. A small inclusion with a diameter ≈4 μm, however, was stable even at 800 °C. These small inclusions contain supercritical water, as evidenced by the sharp Raman peak at 3600 cm^{-1}. Via the peak position, the internal pressure in this stable inclusion was estimated to be 90 MPa. Stability may be facilitated by the formation of a hydrated interfacial layer; the different reactivities of the inclusion fluid at different temperatures leads to different interfacial structures at different temperatures. The presented evidence suggests that inclusions with diameter in the range of few μm are the main source of remaining water and hydroxyl groups in thermally treated high purity quartz sand.

1. Introduction

Quartz is the second most abundant mineral in the earth's crust and the main constituent in hydrothermal quartz veins as well as zoned pegmatite bodies (Deer et al., 2013). The latter are often a source of high purity quartz (HPQ) which is an important raw material for the electronic and semiconductor industry. Quartz from small pegmatite bodies has the highest lattice purity, however, it usually needs beneficiation because of the presence of intergrown minerals like feldspar (Aasly, 2008). Upgraded pegmatite based HPQ exhibits extremely low levels of lattice metal impurities (< 20 ppm) (Buttress et al., 2019) and it is used as raw material for the production of crucibles for photovoltaics grade silicon. Despite of the low metal impurity content, this application also requires low levels of hydroxyl groups and molecular water; water or hydroxyls are often present at interfaces, in defects or inclusions (Biró et al., 2016; Fukuda et al., 2009; Aines et al., 1984; Gawel et al., 2020b). Presence of water can lead to hydrolytic weakening by hydrolysis of Si—O bonds (Baron et al., 2015; Stünitz et al., 2017),

* Corresponding author.
E-mail address: in-situ-heat-quartz@the-passivists.org (A. Erbe).

https://doi.org/10.1016/j.mineng.2021.107238
Received 11 March 2021; Received in revised form 13 September 2021; Accepted 27 September 2021

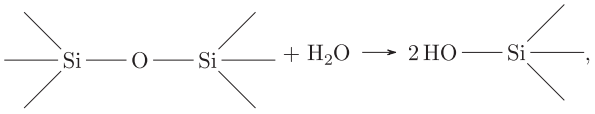

$$\equiv Si - O - Si \equiv + H_2O \rightarrow 2\,HO - Si \equiv, \quad (1)$$

which may lead to deformation of crucibles at high temperature application conditions because of a lowering of quartz glass viscosity. For instance, 24" diameter crucibles are often kept for 100 h at temperatures >1500 °C, while 32" diameter crucibles may have a working life of more than 350 h (Franssila, 2010). Moreover, the presence of hydrogen from water or OH groups triggers the formation of gasses which remain in the crucible in the form of unwanted bubbles. Bubbles present during the pulling of single crystal silicon ingots can lead to a reduction in quality of the silicon product through the formation of crystal defects which can result from the rupturing of the bubble through the crucible surface, thereby reducing the production yield (Sabatino et al., 2017; Yamahara et al., 2001).

One source of water are fluid inclusions. These inclusions are micron-scale cavities which contain paleo-fluids physically trapped within mineral grains in crystal lattice imperfections, in structural holes or channels, or along grain boundaries (Roedder, 1984). In quartz they originate from hydrothermal geological processes during deposition, or from subsequent alteration events such as changes in pressure or temperature. Fluid components in these inclusions are predominantly aqueous solutions with variable concentration of K^+, Na^+ and Cl^-, as well as the gases CO_2, CH_4 and N_2 (Roedder, 1984). Accompanying solid phases are predominantly halite (NaCl) and sylvite (KCl) precipitates (Roedder, 1984) as well as amorphous SiO_2 and feldspars (Thomas et al., 2012).

Upon heating a mineral grain which contains a liquid inclusion, the inclusion may rupture or decrepitate when the internal pressure of the fluid exceeds the confining pressure of the surrounding mineral grain. Partial or full decrepitation events may be observed. The decrepitation temperature is controlled by parameters such as size and shape of the inclusions as well as properties of the host grain. Typically, fluid inclusions in quartz begin to rupture at temperatures below 600 °C with two main stages: the first one between 150 °C and 500 °C, and the second one at 573 °C (Barker and Robinson, 1984). At the latter temperature, the α-β quartz phase transition occurs (Barker and Robinson, 1984). At temperatures above 374 °C and pressures above 22 MPa, water exists in the supercritical state (Wagner and Pruß, 2002). It is likely that reaction between quartz and supercritical water leads to the formation of new hydroxyl species (Walther, 1986).

Clay inclusions are often a source of hydroxyl groups and a source of the Al content in HPQ (Li and Chou, 2015). Moreover, metal ion impurities are also present in quartz lattices as point defects (Götze and Möckel, 2012). These defects often can be recognised by the presence of OH stretching bands in the infrared (IR) spectrum (Rovetta et al., 1989; Aines et al., 1984). Traditionally, the IR bands are assigned to Al-OH stretching vibrations (Aines et al., 1984), however, some authors suggest the presence of "hydrous point defects" in which water molecules inside defects have hydrogen bonds (HBs) to neighbouring atoms, similar to crystal water in hydrous minerals (Koch-Müller et al., 2005). These kinds of structures have been found in nominally anhydrous minerals like olivine and forsterite (Wallis et al., 2019; Padrón-Navarta et al., 2014). However, there is little information about their presence in quartz and in particular HPQ. At the interface H_2O/SiO_2, by using vibrational spectroscopic imaging, a diffuse interfacial layer of a thickness of several μm has been shown to develop at room temperature (Bergonzi et al., 2016). This observation indicates the possibility of chemical reactions even at room temperature. An individual "model" inclusion of water in quartz was studied recently by Raman spectroscopy, and supercritical water was shown to develop at sufficiently high temperatures (Zhou et al., 2019). The study of model water inclusion in quartz during cooling enabled an exploration of regions of the water phase diagram which are otherwise hard to access (Krüger et al., 2019), and showed spectra of strongly hydrogen bound H_2O in ice. Details about the spectral features of water and surface hydroxyls will briefly be summarised in Section 2.

As these examples show, vibrational spectroscopy based methods are often methods of choice for the study of fluid inclusions, e.g. (Fries and Steele, 2018). While the last decade saw an exploding number of studies of fluid inclusions in minerals, many of them also using vibrational spectroscopy, we are not aware of any in situ studies for processed HPQ in powder form. HPQ is a particular challenging substrate for such studies, as it contains only few fluid inclusions and many of the preparation techniques for cross sections as used to study inclusions in extended, macro-scale mineral samples are not suitable. The difficulties of microscopic inspection of these few inclusions highlights the need for "chemical" methods for water detection, as discussed e.g. for the example of structural water by (Sheng et al., 2016). The birefringence of quartz leads to specific challenges concerning quantification (Caumon et al., 2020).

Recently, we have studied the effect of thermal, chemical and mechanical treatment of adsorbed and inclusion water in high purity natural quartz (Gawel et al., 2020b). Inclusions were imaged by Raman spectroscopy, and water removal by temperature treatment characterised via post treatment IR, Raman and NMR spectroscopy (Gawel et al., 2020b). Even after heat treatment to up to 600 °C, significant fractions of the water inclusions were still present in the quartz. The mechanism of its removal and the reactions between water and SiO_2 at higher temperature could, however, not be elucidated only from post mortem investigations. On a general level, in situ studies circumvent the problem of system changes during transfer from the treatment environment to the analysis (Erbe et al., 2016; Erbe et al., 2018).

In this work, we applied in situ IR spectroscopy and Raman microscopy during heating of high purity natural quartz up to 800 °C. Inspired by the processing issues discussed above, we present an analysis mainly of the OH stretching mode region of the spectrum. These experiments shall enable the investigation of formation and condensation of various hydroxyl species which exist only in a certain temperature range. The focus is thus on the spectral features observed with changing temperature, their decomposition using e.g. multivariante curve resolution (MCR), spectrum interpretation, and the structural implications of this interpretation. This work shall neither focus on a full geochemical study of the complete composition of the inclusion fluids, nor on a full analysis of all the information contained in the spectra.

2. Important features of the vibrational spectrum of water and hydroxyls in HPQ

Water and OH groups have been studied extensively by vibrational spectroscopy, but different interpretations of the water spectrum exist (Schmidt and Miki, 2007; Max and Chapados, 2002; Max and Chapados, 2009; Auer and Skinner, 2008), which have been summarised recently (Gawel et al., 2020b). By combining in situ IR spectroscopy with multivariate data analysis, specific water spectral features which change with electrode potential in an electrochemical environment could be extracted, peaking at 3350 and 3240 cm^{-1} (Niu et al., 2017; Niu et al., 2018). In addition to the modes of liquid water, surface water, and OH groups which were extensively discussed in (Gawel et al., 2020b), in situ temperature dependent measurements may yield spectra of water in the gas phase or, above the critical point, of supercritical water. At room temperature, the spectrum of gaseous water is dominated by the symmetric stretching mode at 3654–3657 cm^{-1} (Penney and Lapp, 1976; Frantz et al., 1993; Walrafen et al., 1999; Zhou et al., 2019). With increasing temperature, this peak shifts to lower wavenumber (Walrafen et al., 1999). The exact position is closely related to the density of the developing fluid (Yasaka et al., 2007; Ikushima et al., 1998; Frantz et al., 1993).

The DRIFT spectrum of a typical HPQ sample is shown in Fig. 1. Because of strong absorption from overlapping Si—O related bands

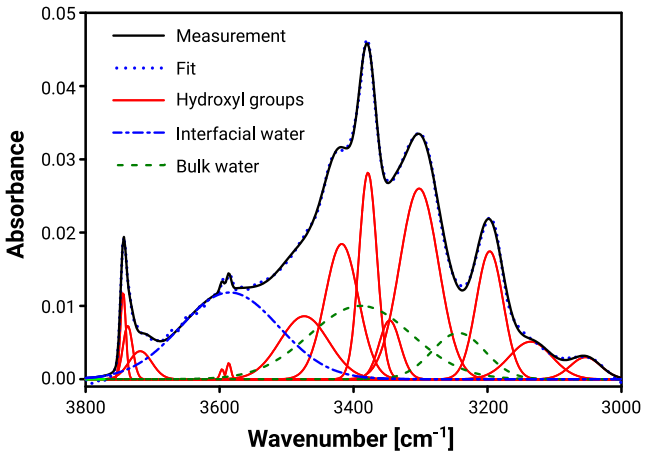

Fig. 1. IR spectrum of typical HPQ sample with peak fitting (envelop line). Peaks assigned to hydroxyl groups (mostly Si—OH), the OH stretchinng mode of interfacial water and from bulk water are shown with different line types. Figure based on (Gawel et al., 2020b).

(including overtones) below 3000 cm^{-1}, only the range between 3800 cm^{-1} and 3000 cm^{-1} of the absorption spectrum of the quartz samples was used. This region mainly comprises the OH stretching modes. The assignment has been discussed in detail elsewhere (Gawel et al., 2020b). The bands can be divided into 5 main groups:

- Non-HB and weak HB surface silanol groups at wavenumbers 3750 cm^{-1} and 3720 cm^{-1} (Dalstein et al., 2017);
- H-bound silanol indicated by the presence of a band between 3700 cm^{-1} to 3650 cm^{-1} (Gallas et al., 2009), only present in non-calcined samples;
- Molecular water, including adsorbed water, with broad features; Peak at 3600 cm^{-1} assigned to surface-bound water (Comas-Vives, 2016; Gaigeot et al., 2012), peak at 3470 cm^{-1} to Si—OH with HB to water, peaks at 3375 cm^{-1} and 3246 cm^{-1} to water with HB-patterns corresponding to the liquid state (Schmidt and Miki, 2007; Max and Chapados, 2002; Auer and Skinner, 2008; Bergonzi et al., 2014; Maréchal, 2011);
- Defect related bands; Peak at 3595 cm^{-1} identified as the B-OH stretching mode (Thomas et al., 2009; Jollands et al., 2020), band at 3585 cm^{-1} as related to OH groups in dislocations (Stalder and Konzett, 2012) or OH^- defect (Jollands et al., 2020), sharp peaks at 3420 cm^{-1}, 3374 cm^{-1} and 3310 cm^{-1} as related to Al-rich defects (Aines et al., 1984; Hadjiivanov, 2014; Jollands et al., 2020);
- Si—O overtones; Peak at 3200 cm^{-1} difficult to assign, however, is likely attributed to Si—O overtones (Thomas et al., 2009);
- Solid inclusion related bands; Peaks at 3146 cm^{-1} and 3035 cm^{-1} are rarely discussed in literature, however these bands could be related to the presence of clay-like solid inclusions (e.g. muscovite) (Kronenberg et al., 2017).

3. Materials and methods

Raw and processed data from this study is available online (Gawel et al., 2020a).

3.1. Materials

HPQ samples used in this work were prepared at The Quartz Corp from ore originating from the Spruce Pine deposit, North Carolina, USA. The originally mined ore was subjected to a series of controlled processing steps like crushing, flotation, acid leaching and thermal treatment. The final quartz product was a powder with 230 μm median diameter, with <10% of particles larger than 400 μm and <10% smaller than 120 μm and more then 99.99% purity. More details on the sample treatment and the trace element impurities are available elsewhere (Gawel et al., 2020b).

3.2. Methods

3.2.1. DRIFT spectroscopy

In situ DRIFT experiments were performed using a Vertex 80v spectrometer (Bruker) fitted with a Praying Mantis accessory and a high temperature reaction chamber (Harrick). The setup consists of a Harrick Temperature Controller (HTC) operated from a computer using the TempLink software designed to link the HTC and Bruker's OPUS software which is used to control the spectrometer. This combination enables an automatisation of temperature dependent in situ experiments. DRIFT Spectra were acquired by averaging 100 scans at 4 cm^{-1} resolution using a liquid nitrogen cooled Mercury Cadmium Telluride (MCT) detector.

The spectrometer was equipped with a homemade add-on to assure vacuum in the sample compartment of the instrument during the experiments. At the same time, argon feed through lines were available to control the atmosphere in the Praying Mantis chamber.

Measurements were preformed every 50 °C or 100 °C between room temperature and a nominal temperature of 700 °C. Since the temperature sensor wasn't placed inside the quartz sample, but below the sample holder in the in situ chamber, the actual temperature of quartz was slightly lower. The difference was up to 50 °C and the deviation was largest at high temperatures.

Collected reflectance spectra measured at different temperatures were divided by a reference spectrum of KBr powder (FTIR grade, Alfa Aesar) measured at room temperature. The baseline of these normalised spectra was fitted with a polynomial which was then subtracted. Finally, the spectra were converted to absorbance.

Peak fitting of the spectra was performed using the software Fityk (Wojdyr, 2010). Multivariate analysis was performed with the software Unscrambler (https://www.camo.com/unscrambler/). The standard multivariate curve resolution with the alternating least squares (MCR-ALS) algorithm from Unscrambler was used. For analysis, absorbance spectra measured at room temperature were used within the range between 4000 cm^{-1} and 3000 cm^{-1}, with the constraint of non-negative concentrations and spectral intensities for all components. The spectral window was limited on the low wavenumber side by the onset of strong harmonic absorption from SiO_2. Most of the variance of the OH stretching mode region spectra was described based on 3 components.

3.2.2. Raman spectroscopy

In situ Raman spectroscopy experiments were performed using a general purpose confocal Raman microscope (Alpha 300 R, WiTec) in a backscattering geometry. The same high temperature reaction chamber (Harrick) used in the DRIFT experiments was used here in a configuration equipped with a flat glass window on top suitable for Raman experiments. The spectra were collected over a range from 100 cm^{-1} to 3800 cm^{-1} with a spectral resolution of 1 cm^{-1} at an excitation wavelength of 532 nm (frequency-doubled Nd-YAG laser operating at 66 mW power). Illumination and detection were performed through a microscope objective of 50× magnification, numerical aperture of 0.75. The experiments were performed between room temperature and nominally 800 °C. Both point measurements and mapping at room temperature were performed, and only point scans at elevated temperatures as spectral mapping was prone to technical challenges in the in situ cell. The resulting hyperspectral images were analysed using the True Component Analysis algorithm implemented in WiTec Control 5.2 software.

MCR analysis as described in Section 3.2.1 was also performed for Raman data; in this case the range was between 3800 cm^{-1} and 3000 cm^{-1}. The same constrains and number of components as for the IR spectra (Section 3.2.1) were used.

4. Results

4.1. Characterisation of HPQ sand at ambient conditions

A micrograph of a quartz sample is shown in Fig. 2A, with an arrow marking a water inclusion. The diameter of this inclusion is ≈2 μm and it is barely discernible in the visual image. This situation is typical for the investigated quartz powder; because of the small size and location under the quartz surface both bright and dark field microscopy gave very low contrast. The presence of imaging artefacts, the diameter in the low μm region and the presence of empty inclusions make the visual detection of fluid containing inclusions even more difficult.

A Raman spectrum of this inclusion is presented in Fig. 2B. The spectrum shows only quartz related modes (McMillan and Hess, 1990; Ichikawa et al., 2003) and weak bands in the OH stretching mode region between 3000 cm^{-1} and 3800 cm^{-1}.

To separate the different dominating components in the Raman spectrum, Raman mapping with analysis of components using the TrueComponent analysis of the instrument's control software was performed. Results from an image are shown in Fig. 3; spectra are available in the data package (Gawel et al., 2020a). These images show 3 main components. Component 1 fills the area around the inclusion and shows

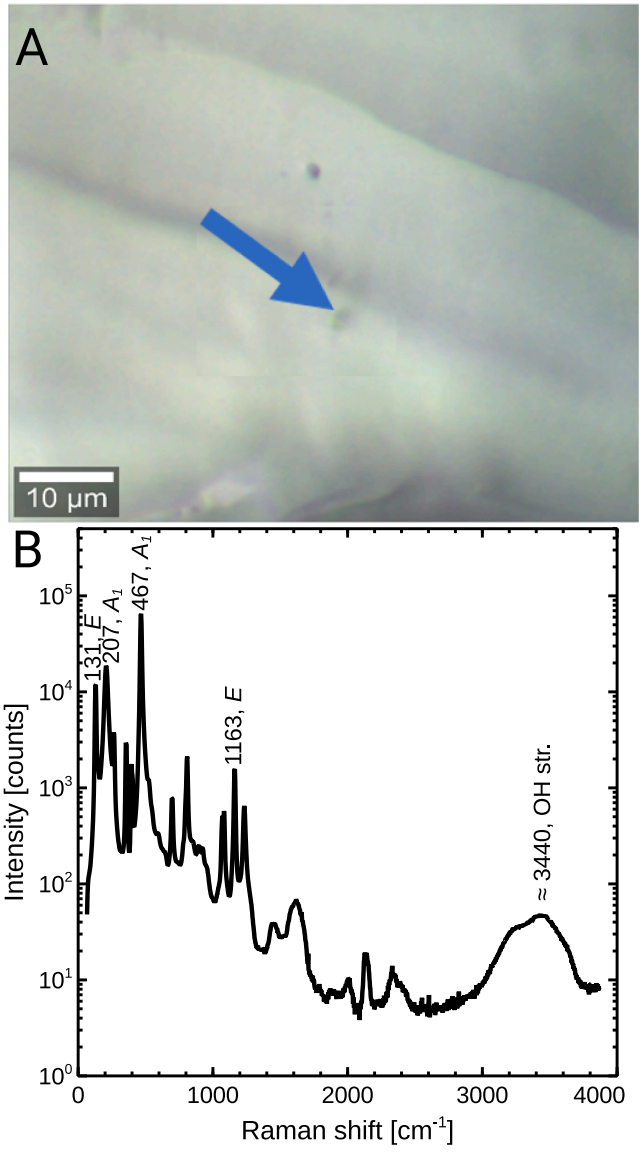

Fig. 2. (A) Micrograph of HPQ, a water inclusion is marked with an arrow. (B) Corresponding Raman spectrum of the region containing the inclusion shown in (A); a constant offset slightly below the minimum measured intensity was subtracted from the measured intensity. Assignment of important characteristic modes is shown together with the observed peak wavenumber.

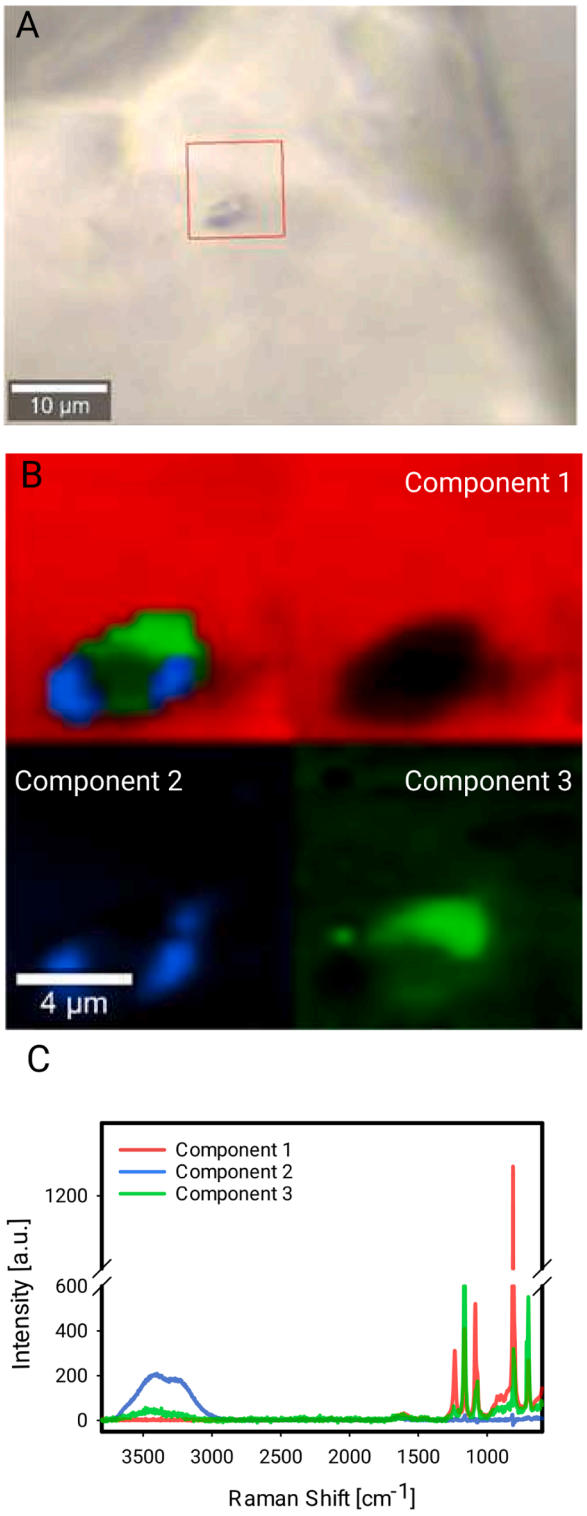

Fig. 3. Raman mapping of a mixed water/SiO_2 containing solid inclusion. A - Microscopy image; B - Raman map from the highlighted area in A, showing the distributions of the components with the spectra shown in C; C - Spectra of the identified components using the instrument control software's TrueComponent analysis (Component 1 - Quartz, Component 2 - Water, Component 3 - SiO_2-based solid inclusion).

only peaks from quartz, as e.g. (Etchepare et al., 1974; McMillan and Hess, 1990; Dolino and Vallade, 1994). Component 2 contains the typical spectrum of liquid water with broad peaks in the OH stretching and bending mode regions, and no sharp peaks. Component 3 is dominated by the sharp modes of quartz, but in a significantly different intensity ratio as component 1. Component 3 is located around the fluid inclusion mainly consisting of water. There are no additional peaks present in this component that would point to the presence of e.g. salts. The difference in intensity of the modes between the main quartz component (component 1) and the solid inclusion component (component 3) is likely related to the presence of a quartz phase with a different crystallographic orientation, also, possibly, with an amorphous component. Component 3 contains in addition a weak peak at ≈3500 cm^{-1}, indicating the presence of OH in this solid phase. The minor peaks in the region between 1250 and 3000 cm^{-1} are present in component 1, i.e. distributed throughout the matrix, with exception of the OH_2 bending mode, which is as expected present in component 2 (details see (Gawel et al., 2020a)). In this inclusion, there is thus no evidence for the presence of other inclusion fluids.[1] The minor peaks between 1250 and 3000 cm^{-1} are thus most likely combinational modes or harmonics from quartz. The size of the inclusion in this case was about 5 × 2 μm^2. Water (Component 2) was present inside the inclusion but it filled only a minor part of it. The solid component (Component 3), however, was the major component in this inclusion.

4.2. *In situ characterisation of liquid inclusions in heat treated HPQ samples*

4.2.1. *Raman mapping*

Fig. 4 shows a series of micrographs containing a highlighted water inclusion, recorded at different temperatures. While the inclusion is round initially, it changes shape between 200 and 400 °C. Raman spectra recorded at the inclusion position (Fig. 5) at room temperature showed a spectrum which clearly resembles the spectrum of liquid water, e.g. (Walrafen et al., 1999; Auer and Skinner, 2008). The peak maximum gradually shifted toward higher wavenumbers with increasing temperature. At 400 °C, only a narrow peak at 3645 cm^{-1} is

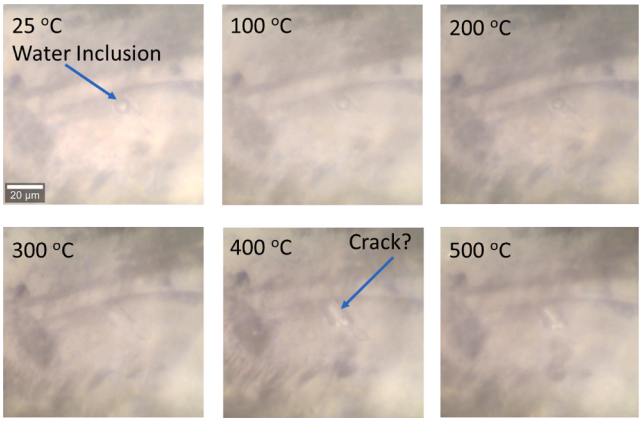

Fig. 4. Micrographs of an inclusion in quartz grains acquired at different temperatures as indicated in the respective panel. Corresponding Raman spectra of the inclusion are shown in Fig. 5.

[1] When comparing spectra to the spectra of other typical inclusion fluids such as CH_4, CO_2 and N_2, e.g. (Naglik et al., 2017; Caumon et al., 2020; Hagiwara et al., 2021), only the peak at ≈ 2330 cm^{-1} matches approximately the position of the NN stretching mode in N_2, however, the observed peak is much wider than the peak of a gaseous N_2 stretching mode.

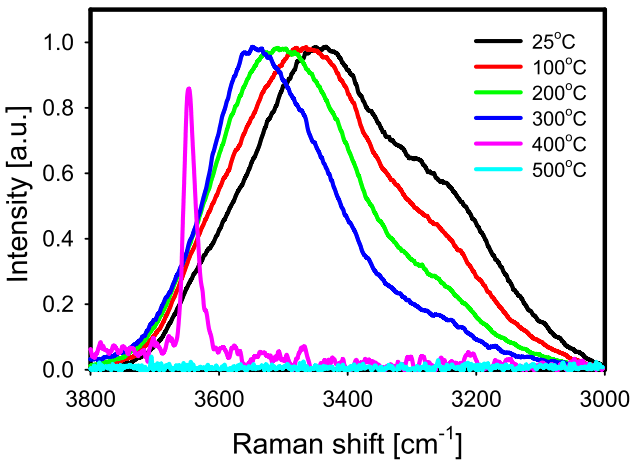

Fig. 5. In situ Raman spectra of the inclusion shown in Fig. 4 heated from room temperature up to 500 °C. Intensities up to 400 °C have been normalised to the maximum intensity with a subsequent baseline subtraction. At 500 °C, no OH stretching mode was detected; the intensity scale for this spectrum is the same as for the 400 °C spectrum..

present, indicating the absence of strong hydrogen bonds. In Section 5.2, this peak will be assigned to the symmetric stretching mode of a fluid close to or above the critical point.

At 500 °C, no signs of water were recorded in the spectra, which means that all water leaked from the inclusion likely through a crack which is shown to develop in Fig. 4. This inclusion also showed spectral signatures of gaseous CO_2 and N_2, with sharp peaks at 1390 and 2330 cm^{-1}, respectively, e.g. (Hagiwara et al., 2021); c.f. (Gawel et al., 2020a) for the full spectra. At the lower temperatures in this series, the integrated intensities of the CO_2 were ≈1% of the water intensities. Even if we take into account the fact that at 532 and 514 nm excitation wavelength, respectively, the Raman scattering cross section per molecule of liquid H_2O (Plakhotnik and Reichardt, 2017) is ten times as high as for the 1390 cm^{-1} CO_2 peak (Penney et al., 1972), liquid water is still by far the dominating species. A full quantification of the different spectral components is even more challenging than described by (Caumon et al., 2020) due to the powdered nature of the samples and was thus not attempted. The intensity of N_2 was only slightly above the noise level at the lower temperatures. The characteristic peaks of CO_2 and N_2 are below the noise level at 500 °C.

In Fig. 6, a micrograph and Raman maps before and after in situ heat treatment experiments at 800 °C are presented. The Raman maps highlight the distribution of water around a water inclusion with a diameter of ≈4 μm. In this case, water was present also after treatment at 800 °C. The location of the water inclusions was shifted compared to the original map. The shape of the water peaks used for the maps were similar in both cases.

Fig. 7 shows Raman spectra of one of the smaller inclusions. The spectra were similar to those shown in Fig. 5. The water peak maximum was shifted with temperature towards higher Raman shift. However, at 700 °C and 800 °C, a band at ≈3600 cm^{-1} was observed which is different than the OH stretching mode at about 3645 cm^{-1} observed in the larger inclusions at lower temperature (Fig. 5). This peak will in Section 5.2 be assigned to supercritical water. In the spectra from this inclusion, no signatures indicating the presence of CO_2 or N_2 were detected.

An MCR analysis of the spectra from Fig. 7A shows three main components (Fig. 7B) and their contributions (Fig. 7C). Component 1 with maximum at 3600 cm^{-1} increases its contribution at 400 °C. Its assignments will be discussed at length in Section 5.2. Component 2, with its main contributions at 3400 cm^{-1} and 3240 cm^{-1} is close to the typical spectrum of liquid water. The intensity of this component vanishes above 400 °C. Component 3 contributes mainly to the spectra

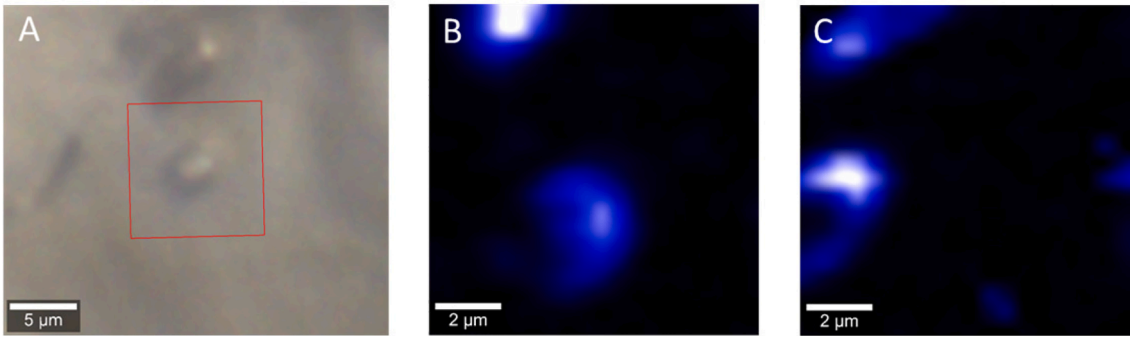

Fig. 6. Micrograph of quartz grain (A) with corresponding Raman scanning maps of the area indicated by a red square in (A) before (B) and after (C) heat treatment at 800 °C. Raman maps represent false colour images obtained as output of the instrument software's True Component Analysis. Blue colour represents a component identified as liquid molecular water based on the shape of the spectral features.

between 200 °C and 600 °C, and will in Section 5.2 be assigned to the presence of surface silanols.

4.2.2. DRIFT spectroscopy

Spectra from in situ heating experiments are shown in Fig. 8. The largest decrease of absorbance was observed near 3400 cm^{-1} (Fig. 8B), related to removal of molecular liquid water from inclusions (Section 4.1). This observation is in line with expectations based on literature (Stünitz et al., 2017; Fukuda et al., 2009; Gallas et al., 2009). Furthermore, removal of species at 3650 cm^{-1} associated with bridged OH species at grains boundaries was also observed. Along with removal of water, new peaks were observed at 3720 cm^{-1} and 3750 cm^{-1}. These peaks indicate the formation of new terminal bridged hydroxyl groups and non-HB hydroxyl species, respectively (Section 4.1). Peaks related to Al-rich defects were stable even at 700 °C.

MCR analysis results of the DRIFT spectra are presented in Fig. 9. Fig. 9A shows the resulting component spectra, while Fig. 9B shows the relative content of each component. This content is estimated based on the unrealistic assumption of equal molar absorption coefficients of different components and may differ from actual composition. A comparison of the spectra with the peak assignments shows the nature of the different components. At the same time, such a comparison also aids a validation of the assignments presented in Section (Section 4.1). Component 3 is related to Al-rich defect related OH species. Component 2 represents molecular and confined water, and component 1 isolated and HB hydroxyl groups. The temperature dependence (Fig. 9B) showed that Al-rich defect OH groups content did not change significantly during heat treatment while water content was decreasing. The highest change was observed at temperatures above 600 °C which corresponds to the "dewatering peak" reported previously in literature (Barker and Robinson, 1984; Kendrick et al., 2006). An important observation was that the Si—OH component increased from 200 °C until 600 °C. The onset of the increase corresponds to the onset of the decrease in the molecular water content. This behaviour is a sign of hydrolysis reaction (1).

The relative content of the Si—OH component, component 1, decreased above 600 °C. In this temperature range, the majority of the water was removed from inclusions, and thus, condensation reactions of OH in appropriate geometric arrangement may be stimulated. It is likely that most of these reactions occur at the inside of previously water-filled inclusions.

The spectrum of component 2, representing molecular liquid water, also contains a peak related to the presence of silanols bound to water likely inside inclusions (peak at 3650 cm^{-1}). The spectrum of component 1 showed not only peaks above 3700 cm^{-1}, but also in the range 3100 cm^{-1} to 3400 cm^{-1}, which are typically associated with Al-rich defects (Section 4.1). There is thus a significant overlap between the spectral components in the spectra of components 1 and 3. The fact that MCR analysis groups some of the peaks of the OH in Al-rich defects together with unbound Si—OH may be an indication that a fraction of the Al-OH rich defects changes in the same manner as Si—OH groups on the surface. The occurrence of these peaks in both components is also a clear sign of the limitations of MCR in this case.

5. Discussion

5.1. Weighting differences between DRIFT and Raman

The Raman and DRIFT spectra showed significant differences, which are related not only to the different selection rules, but also to the different sensitivity and averaging in the two different methods. Raman experiments show mostly water related modes whereas in DRIFT, bands related to OH groups were also present. Raman spectroscopy is highly suited to investigate the majority species in the illuminated, localised area on the order of 1 μm. DRIFT on the other hand gives an average, possibly representative information over the complete sample, including interfacial contributions which are difficult to elucidate from Raman. DRIFT is a highly sensitive method, thus, overtones of the Si—O modes make it challenging to analyse the region below 3000 cm^{-1}.

Because of its high sensitivity towards interfacial species, DRIFT spectra naturally show signatures of surface OH groups. In some cases, multivariate analysis of inclusions gave the possibility to identity also corresponding OH modes in Raman maps. In our experiments, silanols groups were detected along with water in the investigated inclusion.

5.2. Assignment of OH spectral features

The DRIFT spectra can be understood based on the assignment previously reported and summarised in Section 2 (Gawel et al., 2020b). Also the MCR components did not reveal new features.

Raman spectra of individual inclusions at room temperature show the typical spectral signature of liquid water, which shall not be discussed here in detail. In line with a series of investigations of the water to temperatures above the critical point (Frantz et al., 1993; Walrafen et al., 1999; Ikushima et al., 1998; Yasaka et al., 2007; Zhou et al., 2019), the peak maximum moves to higher wavenumbers with increasing temperature, while the peak becomes narrower. We will argue here that in both inclusions, the sharp and clearly visible peak at the highest temperatures is an indication of the symmetric stretching mode of supercritical water inside the inclusion. For both inclusions, the absence of a second, separated maximum indicating a pure gas phase is the strongest argument for the presence of supercritical water in the inclusions.

The 8 μm inclusion showed a peak at 3645 cm^{-1} at 400 °C, and no water peak at 500 °C. At a temperature above the critical temperature, the peak is below the room temperature gas phase peak position of ≈3655 cm^{-1} (Walrafen et al., 1999). Data from (Frantz et al., 1993) shows at 401 °C a peak at 3640 cm^{-1} at a pressure of 23.4 MPa, i.e. slightly above the critical pressure. Data from (Ikushima et al., 1998)

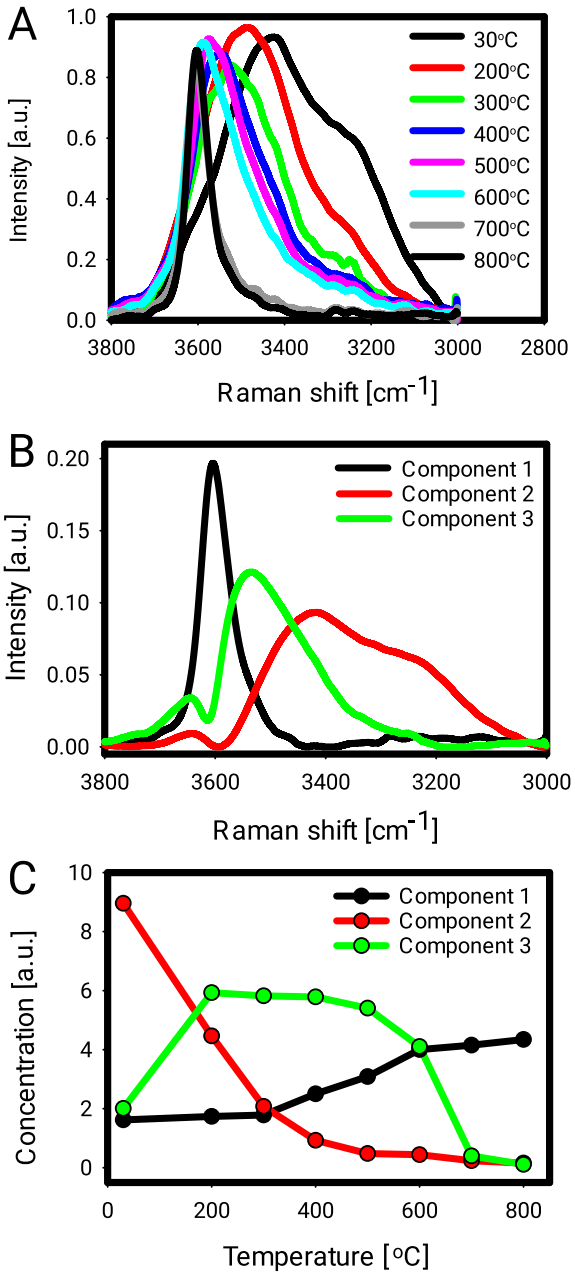

Fig. 7. A – In situ Raman spectra of an inclusion in HPQ with a diameter of ≈4 μm recorded from room temperature up to 800 °C. B – Component spectra obtained from MCR analysis of the spectra in A. C – Temperature-dependent arbitrary scaled concentration of components displayed in B.

shows at 375 °C peaks slightly below 3650 cm^{-1} around the critical pressure. On the other hand, data from (Yasaka et al., 2007) shows for 400 °C that a peak at ≈3645 cm^{-1} corresponds to a density of ≈0.05 g cm^{-3}, indicating a pressure of ≈13 MPa (Wagner and Pruß, 2002; Orlov and Ochkov, 2013) which is below the critical pressure. (Yasaka et al., 2007) also highlight their disagreement with (Ikushima et al., 1998) for the region around the critical point. As no water vapour spectrum was detected at 500 °C in our experiment, but water vapour at ambient densities must have been present, we conclude that the pressure in this inclusion before rupture must have been around the critical pressure of ≈22 MPa. The large fluctuations in the critical region make accurate determinations difficult.

The 4 μm inclusion shows a peak at 3600 cm^{-1} which clearly is indicating supercritical water at 700–800 °C. The data from (Yasaka et al., 2007), in line with earlier studies (Ikushima et al., 1998; Frantz et al., 1993), indicates the presence of a supercritical water phase of a density 0.2 g cm^{-3}. The shape and recording parameters for these peaks were very similar to those for the 8 μm inclusion.

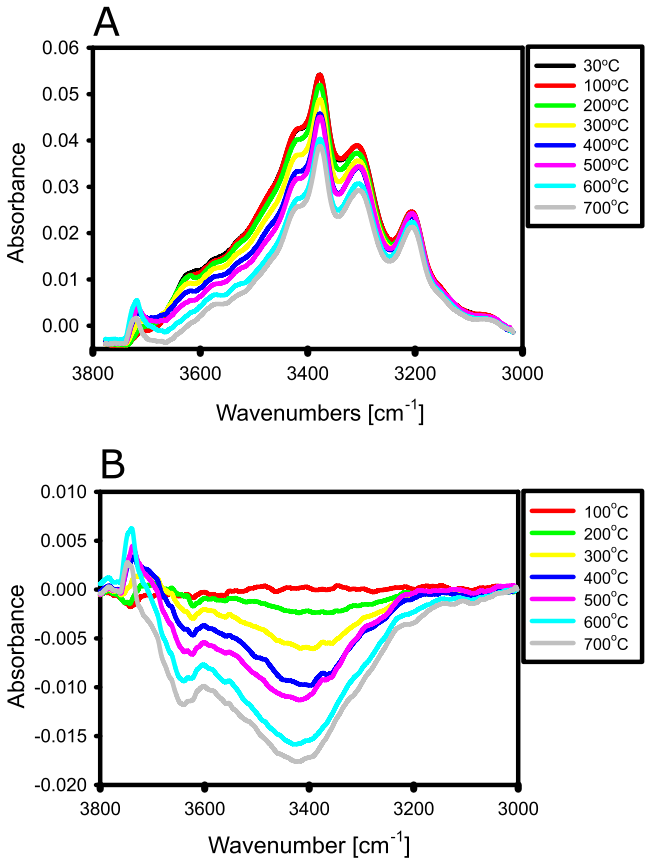

Fig. 8. In situ DRIFT absorbance spectra of HPQ heated from room temperature up to 700 °C. A – Original spectra, B – difference spectra (absorbance at temperature indicated minus absorbance at 30 °C).

The MCR results of the temperature dependent Raman features help in the further assignments of the features by facilitating a deconvolution. Component 2 in Fig. 7 agrees well in shape with the well-known spectrum of liquid water at room temperature (see Section 2). Component 1 in the same figure is the component assigned in the previous paragraph to supercritical water. A component at its peak wavenumber of 3600 cm^{-1} appears to be present also in the liquid water. However, component 2 shows a dip at the peak wavenumber of component 1, and this dip is not present in the spectrum of liquid water. It is thus likely that the dip in the spectrum of component 2 is an MCR artefact, which would imply that the structural reason for the presence of the feature at 3600 cm^{-1} in room temperature liquid water is different from the mode in supercritical water. In room temperature liquid water, this feature has in the IR been assigned to combination of $\nu_1 + \nu_{L2}$ stretching bands of molecular water (Max and Chapados, 2002).

Component 3 (Fig. 7) shows strong contributions at wavenumbers between 3500 and 3600 cm^{-1}. Based on IR assignments for liquid water, its presence at intermediate temperatures could represent a combination of $\nu_1 + \nu_{T2}$ stretching modes (Max and Chapados, 2002), or a mode of undercoordinated water (Bergonzi et al., 2014; Schmidt and Miki, 2007). However, a liquid water component should follow the same temperature dependence as the main liquid water spectrum, and thus, by MCR it should be impossible to separate it from component 2. Thus, we reason here that this component is the same as detected in the IR where it has been assigned to the presence of water molecules H-bound to surface silanols (Gawel et al., 2020b; Gaigeot et al., 2012; Gierada

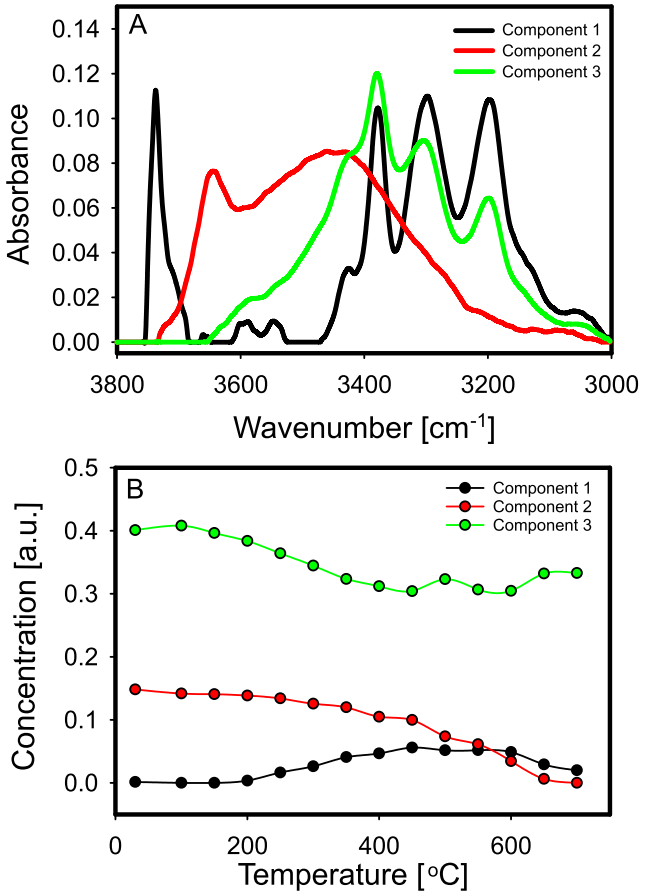

Fig. 9. MCR analysis results of in situ DRIFT absorbance spectra of HPQ heated from room temperature up to 700 °C. A – spectra of three MCR components, B – apparent content of the components.

et al., 2019; Comas-Vives, 2016). While the MCR results of the DRIFT spectra (Fig. 9) do not show a component identical to the component 3 from Raman MCR, the DRIFT component 2 has a very strong absorbance in the region as discussed and is clearly related to surface hydroxyl groups. Surface hydroxyl detection in Raman spectroscopy requires a substantial volume to be filled with the species, i.e. a certain surface roughness or porosity of the internal surface of the inclusions.

5.3. Transformations of water filled inclusions

DRIFT spectra do not display a component that can be attributed to the supercritical water component discussed above. The absence of such a component in DRIFT indicates that formation of supercritical fluid in the inclusions is a distributed event in which different inclusions will rupture at different times or temperatures. Since components at the same wavenumber are also contained in other DRIFT spectra, the special features from "supercritical inclusions" are likely obscured by the many other components.

The close relation between peak wavenumber of the Raman symmetric stretching mode of a water fluid and the density (Frantz et al., 1993; Yasaka et al., 2007; Ikushima et al., 1998) enables an estimate of the fluid density based on the Raman results, assuming the presence of a pure fluid. Using the IAPWS water equation of state (Wagner and Pruß, 2002; Orlov and Ochkov, 2013), the observed density at a set temperature can be used to estimate the maximum pressure p_{max} observed inside the inclusion. These estimates are compiled in Table 1.

It is clear from fundamental physical chemistry that below the critical point, both liquid and gas phase exist. Thus, at room temperature, inclusions may exist which have both a liquid and a gas phase, e.g. (Zhou et al., 2019; Hagiwara et al., 2021). Here, however, such inclusions were not clearly observed, due to the technical challenges getting well-resolved images of these relatively small inclusions, especially in the in situ cell through its top window. Indeed, also quantification has been found challenging for water inclusions $\lesssim$10 μm (Kotov et al., 2021), presumably because of the aperture constraints in their confocal imaging. The inclusions in Fig. 6 may contain both liquid and gas phases. Because of the imaging challenges, the homogenisation temperature could not be determined accurately in this work, which would have been an alternative method to determine when an inclusion reaches the critical point. The fact that the spectra nevertheless show such a transition reveals the strength of the method used here to estimate conditions from the Raman spectra. On the other hand, the Raman method has also disadvantages, discussed and compared e.g. by (Hagiwara et al., 2021). Furthermore, the quartz samples here are processed samples, and the processing may have lead to release of part of the inclusion fluids; indeed, also monophase inclusions have been observed in synthetic inclusions (Qiu et al., 2016).

Table 1
Conditions inside inclusions, assuming in first approximation the presence of pure water. The ≈8 μm inclusion ruptured above the temperature indicated here, while water was still observed in the ≈4 μm inclusion up to the experimental limits in this work.

D[a]	Raman shift[b]	T_{max}[c]	$\rho(H_2O)$[d]	p_{max}[e]
μm	cm^{-1}	°C	g cm^{-3}	MPa
≈8	3645	400	0.05–0.1	13–22
≈4	3600	800	0.2	90

[a] Approximate diameter D of the investigated inclusion.
[b] Raman shift of the water peak at T_{max}.
[c] Maximum Temperature T_{max} at which water was detected.
[d] Density $\rho(H_2O)$ of water from Raman peak.
[e] Maximum pressure p_{max} in inclusion based on IAPWS equation of state (Orlov and Ochkov, 2013).

More information on the pressure on the quartz side of the inclusion could be expected to be obtained from analysis of the main A_1 mode of quartz in the region between 460–470 cm^{-1}, as e.g. shown by (Mercury et al., 2021). Applying the calibration data from (Schmidt and Ziemann, 2000) based on the full width at half maximum of the main quartz A_1 mode did, however, not yield meaningful results, possibly because of a superposition of different contributions. On the other hand, the peak maximum shifted by ≈5 cm^{-1} to lower wavenumbers in the temperature range 25–500 °C, vs. ≈7 cm^{-1} in the quartz reference data (Schmidt and Ziemann, 2000). These differences indicate a difference in stress state and thus pressure.

As the data in Table 1 shows, the 8 μm inclusion ruptured at a lower pressure than present in the 4 μm inclusion; the latter was still stable at significantly higher temperature. While the data presented here has individual character, the observation of small, μm size water inclusions that survive high temperature treatment has also been evidenced in post mortem investigations (Gawel et al., 2020b).

The reasons for the different stability could be related to

1. local differences in mechanical properties of quartz,
2. different microstructure of HPQ around the inclusion,
3. the composition of inclusion fluids,
4. a buildup of a silica interface in the small inclusion which increases mechanical stability, or
5. different reactivities of the fluid at the different temperatures,

which shall be discussed in the following.

(i) Mechanical properties. Many experimental data show that the maximum pressure inside a fluid inclusion depends on its size, shape, composition and density, as well as on the mechanical properties of the host mineral. Pressures of fluid inclusions calculated from rupture

temperatures in various mineral phases (e.g., olivine and quartz) indicate that the fluid overpressure required to cause rupture inversely correlates with the inclusion size; this observation is typically being related to defects in the inclusion surface scaling inversely with size (Bodnar et al., 1989; Wanamaker et al., 1990). Also regimes with negative pressure are important under certain circumstances (Mercury et al., 2021). In this context, the local microstructure must be the underlying reason, see (ii).

(ii) HPQ microstructure. Differences in microstructure around inclusions, such as nature of grain boundaries or vicinity of defects, are likely to contribute to differences in the energetics of inclusions rupturing. With the methods used in this work, no comment on the details of this point can be made. On the other hand, the differences observed here in situ and previously post mortem (Gawel et al., 2020b) are first and foremost related to the size of the liquid domain, and it is not immediately obvious (though via different mechanisms not impossible) that the atomic level details e.g. of a certain grain boundary would be responsible for differences between inclusions on the μm level. Thus, we consider it likely that other mechanisms acting also on the mesoscale must contribute to the differences in rupturing behaviour observed.

(iii) Composition. There is no evidence for significant amounts of salt dissolved in the fluid inclusions in HPQ. Sufficiently high salt concentrations should display by deviations in the bulk liquid spectra, e.g. by shifts of the water OH stretching modes because of the presence of salts in the solutions, e.g. (Wu et al., 2017; Roy et al., 2020). Such differences are not observed, the peak maxima observed here are around 3400 cm^{-1} as for pure water. However, effects are relatively small at moderate salt concentrations (Wu et al., 2017), so that a certain presence of other ions cannot be ruled out.

Furthermore, in the ruptured inclusions, remaining salt deposits should show up in the Raman spectrum e.g. by the characteristic modes of the remaining salts, or the OH stretching modes of hydrated salts, e.g. for NaCl (Burstein et al., 1965; Malley et al., 2018). No such characteristic modes have been found in the data.

(iv) Creation of an amorphous silica interface. A buildup of a silica interface in the small inclusion which likely increases its mechanical stability is possible. As small inclusions are more stable, it is more likely that for those, a hydration of the silica interface will occur. Therefore, a too low calcination temperature may result only in conversion of water into bulk hydroxyl groups instead of their removal, with a formation of a "hydrous" interface after lowering of the temperature. A similar phenomenon has been observed at room temperature (Bergonzi et al., 2016). At higher temperatures in this work, mapping, e.g. of the rim of the inclusions, did not yield meaningful results due to experimental challenges. Therefore, the data presented here is limited to point measurements in the inclusions.

(v) Differences in fluid reactivity. Whether a protective silica layer develops or an inclusion ruptures must necessarily be related to some initiating chemical processes. The fact that the Raman peak position of supercritical water as discussed above depend on density of the fluid is related to structural changes in water with temperature and pressure. Thus, the differences in peak position reflect structural changes of the water inside the inclusions.

Several experimental and simulation techniques shows that hydrogen bonding is present especially at higher densities in supercritical water (Bellissent-Funel, 2001). A model considering supercritical water to consist of clusters with one, two and three H_2O molecules in thermodynamic equilibrium was shown to be consistent with vibrational spectra (Tassaing et al., 2010). A study combining molecular dynamics simulations and Raman spectroscopy lead to the suggestion of tetrahedrally coordinated and linearly coordinated water (Sun et al., 2014). The bending mode, which could not be investigated here easily may be well-suited for structural investigations (Ikeda, 2014).

When the inclusion water observed in this work first enters the supercritical state, this happens at different temperatures in the inclusions of different diameters. While a detailed discussion is beyond the scope of this work, the ≈40 cm^{-1} lower peak frequency of the supercritical water in the 4 μm inclusion indicates the presence of a larger number of H-bound H_2O-molecules. On the other hand, the 8 μm inclusion shows parameters close to the critical temperature and pressure, where the water is still similar to the gas-phase and thus contains significant amounts of mono-and dimers. Under these conditions, thus, more "free", non-H-bound OH groups are available as partners in chemical reactions, e.g. for the hydrolysis of Si—O—Si bond.

Based on the previous discussion, the differences in rupturing conditions of the inclusions may originate from different reactivity of the water once it becomes supercritical. For example, the silica layer discussed in (iii) may form only at higher temperatures at sufficient rates.

The fact that the inclusion which did rupture included CO_2, even though only as minor component, could indicate that the CO_2 is playing a part in the initiation of the rupturing process. For a systematic study, dedicated model inclusion experiments with mixed CO_2/H_2O ratios would be needed. Such studies were not part of this work.

5.4. Role of surface OH groups

DRIFT and Raman spectra show the formation of new hydroxyl groups above 200 °C, i.e. at temperatures below the critical temperature. Surface reactions thus set in in a regime when the inclusion fluid is still liquid. It is likely that formed silanols as "hydrous defect" inside the quartz are far more mobile than molecular water. At higher temperatures, the presence of pores originating from "empty" liquid inclusions and removal of water facilitate also OH removal because of lowering of water vapour pressure inside liquid inclusions.

Inside the inclusions, the forming silanol groups may be a precursor of a silica layer as discussed under (iii) in Section 5.3. As discussed previously, the isolated, non-H-bound OH groups observed in DRIFT up to the highest temperatures can themselves not contribute to further Si—O—Si hydrolysis. However, these groups are always present, may become mobile at temperatures near 1500 °C, could react with each other in a condensation, and the resulting water could elsewhere attack Si—O—Si bonds. On the other hand, thermodynamically there is at best a small driving force for this process. Thus, we reason here that the presence of water in small, stable inclusions will be the main source of inclusion water which may react at temperatures of the Czochralski process.

5.5. Structural reorganisation during heat treatment

Combing the information from the different experiments yields a structural picture as shown in Fig. 10. During thermal treatment, three steps can be distinguished up to the temperature of 800 °C. In the first step, loosely bound water is evaporated from external surfaces. This step proceeds at temperatures around 100 °C (Fig. 10A). After this stage, water is mostly present in inclusions; hydroxyls at the internal interfaces are also present. In the second step, large inclusions rupture, leading to formation of cracks and new surface hydroxyls. In the last step, hydroxyls start to condensate under water release. Only the isolated hydroxyls and small water-filled inclusions remain after heating up to 800 °C. At this temperature water is in the supercritical state.

6. Conclusions

High stability of small (4 μm) inclusions in HPQ grains up to 800 °C was observed. From the peak position of the supercritical water's OH stretching mode, the pressure in this inclusion was determined to be ≈90 MPa. Residual water inclusions may thus play an important role in the behaviour of quartz even at high temperatures. It is also clear that the rupture of larger (down to 8 μm) liquid inclusions is because of a pressure built-up. The single sharp Raman OH stretching mode peak indicates conditions near the critical pressure of ≈22 MPa upon rupture. The fact that the larger inclusion ruptured at 1/3 of the pressure at

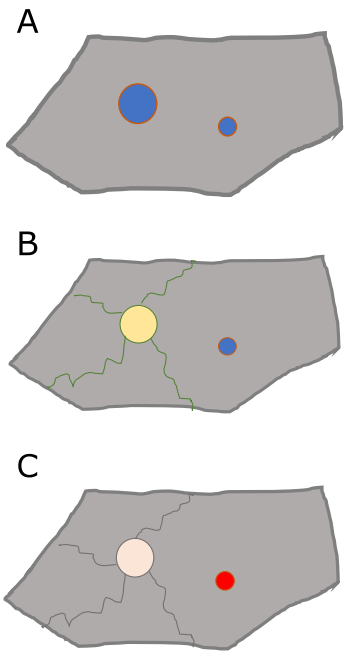

Fig. 10. Overview of inclusion behaviour during heat treatment. Quartz grain after drying at 100 °C (A), 300 °C (B) and 700 °C (C). Water filled inclusions are stable at 100 °C. At 300 °C, the larger inclusions are ruptured and thus empty. At 700 °C, stable inclusions contain supercritical water.

which the smaller inclusion is still stable may be related to different mechanical properties of grains around small inclusions inside quartz grains; the built-up up a silica layer at the solution/quartz interface may have a role in explaining these different mechanical properties. Different reactivities of the inclusion fluid, related to the water structure at the temperatures at which the inclusion fluid becomes supercritical may be the underlying cause of the built-up of this silica layer only in some inclusions. The further role of the internal structure of the investigated grains remains subject to further investigations. In particular, the inclusion which did rupture contained CO_2 as minor component.

Analysing spectroscopic maps with MCR allowed for the detection, likely at the surface of a liquid inclusion, of a layer with OH groups characterised by stretching modes at about 3500 cm^{-1}. This interface was mostly crystalline as evidenced by a sharp peak in the Raman spectrum, however, the presence of an amorphous layer cannot be ruled out. The origin of this interface could be recrystallisation because of changes in temperature and pressure conditions during rock formation. In situ DRIFT showed the formation of new hydroxyls groups at temperatures above 200 °C. These new OH groups must originate from a reaction of water in inclusion with silica at the inclusions surface. Moreover, at temperatures as high as 700 °C, larger inclusions start to rupture. Condensation reactions at the surface free further water and result in the terminal stages in “free”, non-H-bound surface OH groups, clearly evidenced in the DRIFT spectra.

It is likely that water from the thermally stable small inclusion and hydroxyl groups which form in the reaction between water and quartz are the main source of hydrogen at process temperatures of the Czochralski process. The fact that hydrolysis sets in at temperatures as low as 200 °C could be an indication that the actual hydrolytic weakening under process conditions must be related to a mechanism releasing water that was bound at lower temperatures. Candidates for this release, triggering unwanted bubble formation in fused quartz, are the rupturing of smaller inclusions, and the reaction of then mobile previously isolated silanol groups. In order to obtain a full picture of the structural transformations of inclusion water and quartz, an extension of the experiments conducted here to higher temperature will be beneficial.

Data statement

Raw data associated with this study is available via the BIRD repository of Norwegian higher education institutions under https://hdl.handle.net/11250/2775328.

CRediT authorship contribution statement

Bartłomiej A. Gaweł: Data curation, Formal analysis, Investigation, Visualization, Writing – original draft. **Anna Ulvensøen:** Investigation. **Katarzyna Łukaszuk:** Investigation, Project administration, Supervision. **Astrid Marie F. Muggerud:** Conceptualization, Funding acquisition, Project administration, Resources, Supervision, Writing – review & editing. **Andreas Erbe:** Conceptualization, Formal analysis, Funding acquisition, Methodology, Supervision, Writing – review & editing.

Declaration of Competing Interest

The authors declare that they have no known competing financial interests or personal relationships that could have appeared to influence the work reported in this paper.

Acknowledgements

This work was supported by the Research Council of Norway [EngQS project, No. 282341]. We acknowledge Anders Bank Blichfeld for constructing the feed-through system enabling the in situ heating DRIFT experiments.

References

Aasly, K., 2008. Properties and behavior of quartz for the silicon process. Ph.D. thesis. Norwegian University of Science and Technology, Trondheim, Norway.
Aines, R.D., Kirby, S.H., Rossman, G.R., 1984. Hydrogen speciation in synthetic quartz. Phys. Chem. Miner. 11, 204–212. https://doi.org/10.1007/BF00308135.
Auer, B.M., Skinner, J.L., 2008. IR and Raman spectra of liquid water: Theory and interpretation. J. Chem. Phys. 128, 224511. https://doi.org/10.1063/1.2925258.
Barker, C., Robinson, S., 1984. Thermal release of water from natural quartz. Am. Mineral. 69, 1078–1081 https://pubs.geoscienceworld.org/ammin/article-pdf/69/11-12/1078/4217157/am69_1078.pdf.
Baron, M.A., Stalder, R., Konzett, J., Hauzenberger, C.A., 2015. OH-point defects in quartz in B- and Li-bearing systems and their application to pegmatites. Phys. Chem. Miner. 42, 53–62. https://doi.org/10.1007/s00269-014-0699-4.
Bellissent-Funel, M.C., 2001. Structure of supercritical water. J. Mol. Liq. 90, 313–322. https://doi.org/10.1016/S0167-7322(01)00135-0.
Bergonzi, I., Mercury, L., Brubach, J.B., Roy, P., 2014. Gibbs free energy of liquid water derived from infrared measurements. Phys. Chem. Chem. Phys. 16, 24830–24840. https://doi.org/10.1039/C4CP03466J.
Bergonzi, I., Mercury, L., Simon, P., Jamme, F., Shmulovich, K., 2016. Oversolubility in the microvicinity of solid–solution interfaces. Phys. Chem. Chem. Phys. 18, 14874–14885. https://doi.org/10.1039/C5CP08012F.
Biró, T., Kovács, I.J., Király, E., Falus, G., Karátson, D., Bendo, Z., Fancsik, T., Sándorné, J.K., 2016. Concentration of hydroxyl defects in quartz from various rhyolitic ignimbrite horizons: Results from unpolarized micro-FTIR analyses on unoriented phenocryst fragments. Eur. J. Mineral. 28, 313–327. https://doi.org/10.1127/ejm/2016/0028-2515.
Bodnar, R.J., Binns, P.R., Hall, D.L., 1989. Synthetic fluid inclusions - VI. Quantitative evaluation of the decrepitation behaviour of fluid inclusions in quartz at one atmosphere confining pressure. J. Metamorph. Geol. 7, 229–242. https://doi.org/10.1111/j.1525-1314.1989.tb00586.x.
Burstein, E., Johnson, F.A., Loudon, R., 1965. Selection rules for second-order infrared and Raman processes in the rocksalt structure and interpretation of the raman spectra of NaCl, KBr, and NaI. Phys. Rev. 139, A1239–A1245. https://doi.org/10.1103/PhysRev.139.A1239.
Buttress, A.J., Rodriguez, J.M., Ure, A., Ferrari, R.S., Dodds, C., Kingman, S.W., 2019. Production of high purity silica by microfluidic-inclusion fracture using microwave pre-treatment. Miner. Eng. 131, 407–419. https://doi.org/10.1016/j.mineng.2018.11.025.
Caumon, M.C., Tarantola, A., Wang, W., 2020. Raman spectra of gas mixtures in fluid inclusions: Effect of quartz birefringence on composition measurement. J. Raman Spectrosc. 51, 1868–1873. https://doi.org/10.1002/jrs.5605.
Comas-Vives, A., 2016. Amorphous SiO_2 surface models: energetics of the dehydroxylation process, strain, ab initio atomistic thermodynamics and IR spectroscopic signatures. Phys. Chem. Chem. Phys. 18, 7475–7482. https://doi.org/10.1039/C6CP00602G.

Dalstein, L., Potapova, E., Tyrode, E., 2017. The elusive silica/water interface: isolated silanols under water as revealed by vibrational sum frequency spectroscopy. Phys. Chem. Chem. Phys 19, 10343–10349. https://doi.org/10.1039/C7CP01507K.

Deer, W.A., Howie, R.A., Zussman, J., 2013. An Introduction to the Rock-Forming Minerals. Mineralogical Society of Great Britain and Ireland, London, UK. https://doi.org/10.1180/DHZ.

Di Sabatino, M., Thorsen, F.W., Lanterne, A., Hu, Y., Bones, J.A., Øvrelid, E., 2017. Investigation on quartz crucibles for monocrystalline silicon ingots for solar cells. In: Energy Technology 2017 - Carbon Dioxide Management and Other Technologies. The Minerals. Metals & Materials Society/ Springer, Cham, Switzerland, pp. 387–394. https://doi.org/10.1007/978-3-319-52192-3_38.

Dolino, G., Vallade, M., 1994. Lattice dynamical behavior of anhydrous silica. Rev. Mineral. Geochem. 29, 403–431.

Erbe, A., Nayak, S., Chen, Y.H., Niu, F., Pander, M., Tecklenburg, S., Toparli, C., 2018. How to probe structure, kinetics, and dynamics at complex interfaces in situ and operando by optical spectroscopy. In: Wandelt, K. (Ed.), Encyclopedia of Interfacial Chemistry. Elsevier, Oxford, pp. 199–219. https://doi.org/10.1016/B978-0-12-409547-2.14061-2.

Erbe, A., Sarfraz, A., Toparli, C., Schwenzfeier, K., Niu, F., 2016. Optical absorption spectroscopy at interfaces. In: Lang, P.R., Liu, Y. (Eds.), Soft Matter at Aqueous Interfaces. Springer, Cham, Switzerland. volume 917 of Lect. Notes Phys., pp. 459–490. doi:10.1007/978-3-319-24502-7_14.

Etchepare, J., Merian, M., Smetankine, L., 1974. Vibrational normal modes of SiO_2. I. $\alpha$and βquartz. J. Chem. Phys. 60, 1873–1876. https://doi.org/10.1063/1.1681287.

Franssila, S., 2010. chapter 4 - Silicon. In: Introduction to Microfabrication. Wiley, Chichester, UK, pp. 35–46. https://doi.org/10.1002/9781119990413.ch4.

Frantz, J.D., Dubessy, J., Mysen, B., 1993. An optical cell for Raman spectroscopic studies of supercritical fluids and its application to the study of water to 500C and 2000 bar. Chem. Geol. 106, 9–26. https://doi.org/10.1016/0009-2541(93)90163-D.

Fries, M., Steele, A., 2018. Raman spectroscopy and confocal Raman imaging in mineralogy and petrography. In: Toporski, J., Dieing, T., Hollricher, O. (Eds.), Confocal Raman Microscopy. Springer, Cham, Switzerland, pp. 209–236. https://doi.org/10.1007/978-3-319-75380-5_10.

Fukuda, J., Yokoyama, T., Kirino, Y., 2009. Characterization of the states and diffusivity of intergranular water in a chalcedonic quartz by high-temperature in situ infrared spectroscopy. Mineral. Mag. 73, 825–835. https://doi.org/10.1180/minmag.2009.073.5.825.

Gaigeot, M.P., Sprik, M., Sulpizi, M., 2012. Oxide/water interfaces: How the surface chemistry modifies interfacial water properties. J. Phys.: Condens. Matter 24, 124106. https://doi.org/10.1088/0953-8984/24/12/124106.

Gallas, J.P., Goupil, J.M., Vimont, A., Lavalley, J.C., Gil, B., Gilson, J.P., Miserque, O., 2009. Quantification of water and silanol species on various silicas by coupling IR spectroscopy and in-situ thermogravimetry. Langmuir 25, 5825–5834. https://doi.org/10.1021/la802688w.

Gawel, B.A., Ulvensøen, A., Lukaszuk, K., Arstad, B., Muggerud, A.M.F., Erbe, A., 2020a. Spectroscopic data of water and hydroxyls in high purity natural quartz. BIRD, https://hdl.handle.net/11250/2775328.

Gawel, B.A., Ulvensøen, A., Lukaszuk, K., Arstad, B., Muggerud, A.M.F., Erbe, A., 2020b. Structural evolution of water and hydroxyl groups during thermal, mechanical and chemical treatment of high purity natural quartz. RSC Adv. 10, 29018–29030. https://doi.org/10.1039/D0RA05798C.

Gierada, M., De Proft, F., Sulpizi, M., Tielens, F., 2019. Understanding the acidic properties of the amorphous hydroxylated silica surface. J. Phys. Chem. C 123, 17343–17352. https://doi.org/10.1021/acs.jpcc.9b04137.

Götze, J., Möckel, R., 2012. Quartz: Deposits, mineralogy and analytics. Springer, Heidelberg, Germany. https://doi.org/10.1007/978-3-642-22161-3.

Hadjiivanov, K., 2014. Identification and characterization of surface hydroxyl groups by infrared spectroscopy. Adv. Catal. 57, 99–318. https://doi.org/10.1016/B978-0-12-800127-1.00002-3.

Hagiwara, Y., Yoshida, K., Yoneda, A., Torimoto, J., Yamamoto, J., 2021. Experimental variable effects on laser heating of inclusions during Raman spectroscopic analysis. Chem. Geol. 559, 119928. https://doi.org/10.1016/j.chemgeo.2020.119928.

Ichikawa, S., Suda, J., Sato, T., Suzuki, Y., 2003. Lattice dynamics and temperature dependence of the first-order Raman spectra for α-SiO_2 crystals. J. Raman Spectrosc. 34, 135–141. https://doi.org/10.1002/jrs.966.

Ikeda, T., 2014. Infrared absorption and Raman scattering spectra of water under pressure via first principles molecular dynamics. J. Chem. Phys. 141, 044501. https://doi.org/10.1063/1.4890369.

Ikushima, Y., Hatakeda, K., Saito, N., Arai, M., 1998. An in situ Raman spectroscopy study of subcritical and supercritical water: The peculiarity of hydrogen bonding near the critical point. J. Chem. Phys. 108, 5855–5860. https://doi.org/10.1063/1.475996.

Jollands, M.C., Blanchard, M., Balan, E., 2020. Structure and theoretical infrared spectra of OH defects in quartz. Eur. J. Mineral. 32, 311–323. https://doi.org/10.5194/ejm-32-311-2020.

Kendrick, M., Phillips, D., Miller, J., 2006. Part I. Decrepitation and degassing behaviour of quartz up to 1560 °C: Analysis of noble gases and halogens in complex fluid inclusion assemblages. Geochim. Cosmochim. Acta 70, 2540–2561. https://doi.org/10.1016/j.gca.2005.12.023.

Koch-Müller, M., Dera, P., Fei, Y., Hellwig, H., Liu, Z., Orman, J., Wirth, R., 2005. Polymorphic phase transition in superhydrous phase B. Phys. Chem. Miner. 32, 349–361. https://doi.org/10.1007/s00269-005-0007-4.

Kotov, A.A., Smirnov, S.Z., Plechov, P.Y., Persikov, E.S., Chertkova, N.V., Maksimovich, I.A., Karmanov, N.S., Buhtiyarov, P.G., 2021. Method for determining water content in natural rhyolitic melts by Raman spectroscopy and electron microprobe analysis. Petrology 29, 386–403. https://doi.org/10.1134/S0869591121040044.

Krüger, Y., Mercury, L., Canizarès, A., Marti, D., Simon, P., 2019. Metastable phase equilibria in the ice II stability field. A Raman study of synthetic high-density water inclusions in quartz. Phys. Chem. Chem. Phys. 21, 19554–19566. https://doi.org/10.1039/C9CP03647D.

Kronenberg, A.K., Hasnan, H.F.B., Holyoke III, C.W., Law, R.D., Liu, Z., Thomas, J.B., 2017. Synchrotron FTIR imaging of OH in quartz mylonites. Solid Earth 8, 1025–1045. https://doi.org/10.5194/se-8-1025-2017.

Li, J., Chou, I.M., 2015. Hydrogen in silicate melt inclusions in quartz from granite detected with Raman spectroscopy. J. Raman Spectrosc. 46, 983–986. https://doi.org/10.1002/jrs.4644.

Malley, P.P.A., Chakraborty, S., Kahan, T.F., 2018. Physical characterization of frozen saltwater solutions using Raman microscopy. ACS Earth Space Chem. 2, 702–710. https://doi.org/10.1021/acsearthspacechem.8b00045.

Maréchal, Y., 2011. The molecular structure of liquid water delivered by absorption spectroscopy in the whole IR region completed with thermodynamics data. J. Mol. Struct. 1004, 146–155. https://doi.org/10.1016/j.molstruc.2011.07.054.

Max, J.J., Chapados, C., 2002. Isotope effects in liquid water by infrared spectroscopy. J. Chem. Phys. 116, 4626–4642. https://doi.org/10.1063/1.1448286.

Max, J.J., Chapados, C., 2009. Isotope effects in liquid water by infrared spectroscopy. III. H_2O and D_2O spectra from 6000 to 0 cm^{-1}. J. Chem. Phys. 131, 184505. https://doi.org/10.1063/1.3258646.

McMillan, P., Hess, A., 1990. Ab initio valence force field calculations for quartz. Phys. Chem. Minerals 17, 97–107. https://doi.org/10.1007/BF00199660.

Mercury, L., de Bilbao, E., Simon, P., Raimbourg, H., Bergonzi, I., Hulin, C., Canizarès, A., Shmulovich, K.I., 2021. Quartz stressing and fracturing by pore pressure dropping down to negative pressure. ACS Earth Space Chem. 5, 170–185. https://doi.org/10.1021/acsearthspacechem.0c00224.

Naglik, B., Tobola, T., Natkaniec-Nowak, L., Luptáková, J., Milovská, S., 2017. Raman spectroscopic and microthermometric studies of authigenic quartz (the pepper mts., central poland) as an indicator of fluids circulation. Spectrochim. Acta A 173, 960–964. https://doi.org/10.1016/j.saa.2016.10.047.

Niu, F., Rabe, M., Nayak, S., Erbe, A., 2018. Vibrational spectroscopic study of pH dependent solvation at a Ge(100)-water interface during an electrode potential triggered surface termination transition. J. Chem. Phys. 148, 222824. https://doi.org/10.1063/1.5018796.

Niu, F., Schulz, R., Castañeda Medina, A., Schmid, R., Erbe, A., 2017. Electrode potential dependent desolvation and resolvation of germanium(100) in contact with aqueous perchlorate electrolytes. Phys. Chem. Chem. Phys. 19, 13585–13595. https://doi.org/10.1039/C6CP08908A.

Orlov, K., Ochkov, V., 2013. MPEI's online calculation page - thermodynamic properties of ordinary water substance for general and scientific use. http://twt.mpei.ac.ru/mcs/worksheets/iapws/IAPWS95.xmcd. accessed 24 December 2020.

Padrón-Navarta, J.A., Hermann, J., O'Neill, H.S.C., 2014. Site-specific hydrogen diffusion rates in forsterite. Earth Planet. Sci. Lett. 392, 100–112. https://doi.org/10.1016/j.epsl.2014.01.055.

Penney, C.M., Goldman, L.M., Lapp, M., 1972. Raman scattering cross sections. Nature Phys. Sci. 235, 110–112. https://doi.org/10.1038/physci235110b0.

Penney, C.M., Lapp, M., 1976. Raman-scattering cross sections for water vapor. J. Opt. Soc. Am. 66, 422–425. https://doi.org/10.1364/JOSA.66.000422.

Plakhotnik, T., Reichardt, J., 2017. Accurate absolute measurements of the Raman backscattering differential cross-section of water and ice and its dependence on the temperature and excitation wavelength. J. Quant. Spectrosc. Radiat. Transfer 194, 58–64. https://doi.org/10.1016/j.jqsrt.2017.03.023.

Qiu, C., Krüger, Y., Wilke, M., Marti, D., Ricka, J., Frenz, M., 2016. Exploration of the phase diagram of liquid water in the low-temperature metastable region using synthetic fluid inclusions. Phys. Chem. Chem. Phys. 18, 28227–28241. https://doi.org/10.1039/C6CP04250C.

Roedder, E., 1984. Fluid Inclusions. volume 12 of Rev. Mineral. Mineralogical Society of America, Washington, DC, USA.

Rovetta, M.R., Blacic, J.D., Hervig, R.L., Holloway, J.R., 1989. An experimental study of hydroxyl in quartz using infrared spectroscopy and ion microprobe techniques. J. Geophys. Res. 94, 5840–5850. https://doi.org/10.1029/JB094iB05p05840.

Roy, S., Patra, A., Saha, S., Palit, D.K., Mondal, J.A., 2020. Restructuring of hydration shell water due to solvent-shared ion pairing (SSIP): A case study of aqueous MgCl_2 and LaCl_3 solutions. J. Phys. Chem. B 124, 8141–8148. https://doi.org/10.1021/acs.jpcb.0c05681.

Schmidt, C., Ziemann, M.A., 2000. In-situ Raman spectroscopy of quartz: A pressure sensor for hydrothermal diamond anvil cell experiments at elevated temperatures: Am. Mineral. 85, 1725–1734. https://doi.org/10.2138/am-2000-11-1216.

Schmidt, D.A., Miki, K., 2007. Structural correlations in liquid water: A new interpretation of IR spectroscopy. J. Phys. Chem. A 111, 10119–10122. https://doi.org/10.1021/jp074737n.

Sheng, Y., Gong, B., Li, W., Xia, M., 2016. Methodological progress in trace amounts of structural water in nominally anhydrous minerals. Sci. China: Earth Sci. 59, 901–909. https://doi.org/10.1007/s11430-016-5281-0.

Stalder, R., Konzett, J., 2012. OH defects in quartz in the system quartz-albite-water and granite-water between 5 and 25 kbar. Phys. Chem. Miner. 39, 817–827. https://doi.org/10.1007/s00269-012-0537-5.

Stünitz, H., Thust, A., Heilbronner, R., Behrens, H., Kilian, R., Tarantola, A., Fitz Gerald, J.D., 2017. Water redistribution in experimentally deformed natural milky quartz single crystals — Implications for H2O-weakening processes. J. Geophys. Res. B 122, 866–894. https://doi.org/10.1002/2016JB013533.

Sun, Q., Wang, Q., Ding, D., 2014. Hydrogen bonded networks in supercritical water. J. Phys. Chem. B 118, 11253–11258. https://doi.org/10.1021/jp503474s.

Tassaing, T., Garrain, P.A., Bégué, D., Baraille, I., 2010. On the cluster composition of supercritical water combining molecular modeling and vibrational spectroscopic data. J. Chem. Phys. 133, 034103. https://doi.org/10.1063/1.3457483.

Thomas, R., Davidson, P., Badanina, E., 2012. Water- and boron-rich melt inclusions in quartz from the Malkhan pegmatite. Transbaikalia, Russia. Minerals 2, 435–458. https://doi.org/10.3390/min2040435.

Thomas, S.M., Koch-Müller, M., Reichart, P., Rhede, D., Thomas, R., Wirth, R., Matsyuk, S., 2009. IR calibrations for water determination in olivine, r-GeO_2, and SiO_2 polymorphs. Phys. Chem. Miner. 36, 489–509. https://doi.org/10.1007/s00269-009-0295-1.

Wagner, W., Pruß, A., 2002. The IAPWS formulation 1995 for the thermodynamic properties of ordinary water substance for general and scientific use. J. Phys. Chem. Ref. Data 31, 387–535. https://doi.org/10.1063/1.1461829.

Wallis, D., Hansen, L., Tasaka, M., Kumamoto, K., Parsons, A., Lloyd, G., Kohlstedt, D., Wilkinson, A., 2019. The impact of water on slip system activity in olivine and the formation of bimodal crystallographic preferred orientations. Earth Planet. Sci. Lett. 508, 51–61. https://doi.org/10.1016/j.epsl.2018.12.007.

Walrafen, G.E., Yang, W.H., Chu, Y.C., 1999. Raman spectra from saturated water vapor to the supercritical fluid. J. Phys. Chem. B 103, 1332–1338. https://doi.org/10.1021/jp9831233.

Walther, J., 1986. Mineral solubilities in supercritical H_2O solutions. Pure Appl. Chem. 58, 1585–1598. https://doi.org/10.1351/pac198658121585.

Wanamaker, B.J., Wong, T.F., Evans, B., 1990. Decrepitation and crack healing of fluid inclusions in San Carlos olivine. J. Geophys. Res.: Solid Earth 95, 15623–15641. https://doi.org/10.1029/JB095iB10p15623.

Wojdyr, M., 2010. Fityk: a general-purpose peak fitting program. J. Appl. Crystallogr. 43, 1126–1128. https://doi.org/10.1107/S0021889810030499.

Wu, X., Lu, W., Ou, W., Caumon, M.C., Dubessy, J., 2017. Temperature and salinity effects on the Raman scattering cross section of the water OH-stretching vibration band in NaCl aqueous solutions from 0 to 300 °C. J. Raman Spectrosc. 48, 314–322. https://doi.org/10.1002/jrs.5039.

Yamahara, K., Huang, X., Sakai, S., Utsunomiya, A., Tsurita, Y., Hoshikawa, K., 2001. Surface of silica glass reacting with silicon melt: Effect of raw materials for silica crucibles. Jpn. J. Appl. Phys. 40, 1178–1182. https://doi.org/10.1143/jjap.40.1178.

Yasaka, Y., Kubo, M., Matubayasi, N., Nakahara, M., 2007. High-sensitivity Raman spectroscopy of supercritical water and methanol over a wide range of density. Bull. Chem. Soc. Jpn. 80, 1764–1769. https://doi.org/10.1246/bcsj.80.1764.

Zhou, L., Mernagh, T.P., Le Losq, C., 2019. Observation of the chemical structure of water up to the critical point by raman spectroscopic analysis of fluid inclusions. J. Phys. Chem. B 123, 5841–5847. https://doi.org/10.1021/acs.jpcb.9b02129.